applied sciences

MDPI

Article

Surrogate-Based Optimization of a Centrifugal Pump with Volute Casing for an Automotive Engine Cooling System

Remo De Donno [1], Alessia Fracassi [1,*], Antonio Ghidoni [2], Alessandro Morelli [2] and Gianmaria Noventa [2]

[1] Industrie Saleri Italo S.p.A., Via Ruca 406, 25065 Lumezzane, Italy; remo.dedonno@saleri.com
[2] Department of Mechanical and Industrial Engineering, University of Brescia, Via Branze 38, 25123 Brescia, Italy; antonio.ghidoni@unibs.it (A.G.); a.morelli005@unibs.it (A.M.); gianmaria.noventa@unibs.it (G.N.)
* Correspondence: alessia.fracassi@saleri.com

Abstract: This paper investigates the capability of a surrogate-based optimization technique for the advanced design of centrifugal pumps. The centrifugal pump considered in this work is designed for the automotive cooling system and consists of an impeller, a vaneless diffuser and a volute. A fully three-dimensional geometry parametrization based on Bézier surfaces is presented. The optimization procedure includes the following software packages: Scilab for the geometric parametrization, Ansys-CFX for the CFD simulations and DAKOTA for the optimization management. The initial geometry is defined by a 0D code that provides a preliminary design of the pump, given the operating conditions, i.e., the volumetric flow rate, the head and the rotating speed. In this work an operative point typical of high performance gasoline cars is considered.

Keywords: centrifugal pump; Bézier polynomials; shape optimization; Kriging

Citation: De Donno, R.; Fracassi, A.; Ghidoni, A.; Morelli, A.; Noventa, G. Surrogate-Based Optimization of a Centrifugal Pump with Volute Casing for an Automotive Engine Cooling System. *Appl. Sci.* **2021**, *11*, 11470. https://doi.org/10.3390/app112311470

Academic Editor: Xiaolin Wang

Received: 11 October 2021
Accepted: 21 November 2021
Published: 3 Decmeber 2021

1. Introduction

The role of the centrifugal pump in a car cooling circuit is to guarantee the liquid circulation, and, therefore, to control the engine temperature. The design of a centrifugal pump turns out to be a difficult task for the following reasons: (*i*) the working point varies over a wide range of flow rate and pressure head; (*ii*) automotive companies require ever strict constraints for pump dimensions and geometry coupling, possibly different for each car model. Moreover, traditional design approaches based on empirical correlations or trial and error methods (based on previous developed models) are characterized by low accuracy (the former) and by an excessive time/cost to reach the optimal design (the latter).

Optimization algorithms coupled with Computational fluid dynamic (CFD) have demonstrated to be a robust and automatic alternative in the design of centrifugal pumps [1], which can overcome the limits of the traditional approaches. However, the works available in literature are often characterized by a simple parametrization, a small number of design variables [2,3], and only some components are optimized, i.e., the impeller [2,4–8], or the diffuser [9], or the volute [10].

Centrifugal pumps for the cooling system are characterized by a compact layout to meet the downsizing policies of car makers. The location of the suction pipes is usually prescribed by the engine, and, in general, the vaned diffuser is not adopted because it could decrease the pump performance in off-design conditions. The vaneless diffuser is often used only as a connection between the impeller and the volute. A typical pump geometry is made of an impeller, a small vaneless diffuser, and a volute. The objective of this work is to propose an automatic methodology based on the shape optimization to design from scratch a centrifugal pump for the automotive field. A preliminary work has been presented in [11], where some limitations are present: (*i*) a baseline design is not available in an automatic manner and, as a consequence, the range of the design space is difficult to set and can be too wide to be spanned with a genetic algorithm; (*ii*) the vaneless diffuser represents only the gap created by the parametrization of the impeller, and the

volute, i.e., it cannot be controlled directly by the optimization process, and (*iii*) the volute cross section is free to change and its boundaries are parametrized with Bézier curves. The latter choice allows the optimization process to find cross sections with "original" shapes, which are often difficult and/or expensive to manufacture. For these reasons, the approach proposed in [11] has been extended. A baseline geometry is generated by a lumped parameter code and optimized with respect to the efficiency with a genetic algorithm. The optimized baseline geometry is parametrized and the 3D model of the pump is created. Finally, a surrogate based optimization strategy is used to optimize the 3D geometry (impeller, vaneless diffuser, and volute).

2. Problem Formulation

The operating conditions (see Table 1) of the pump to design are provided by the Italian company Industrie Saleri Italo S.p.A. (http://www.saleri.com/, accessed on November 2021), as a representative working point for a high performance gasoline car.

The objective is to design a pump that satisfies the operating conditions and maximize the hydraulic efficiency. In particular, the design must guarantee a prescribed total pressure rise Δp_t to ensure the proper flow rate in the cooling circuit. Δp_t is equal to $p_{t4} - p_{t0}$, where p_{t4} is the total pressure at the volute outlet and p_{t0} the total pressure at the suction pipe. The hydraulic efficiency is defined as follows:

$$\eta = \dot{Q}\Delta p_t / W, \tag{1}$$

where $\dot{Q}$ [m^3/s] is the volumetric flow rate and W [W] the power at the impeller. The total pressure head value reported in Table 1 is constrained in the range $\pm$5% during the optimization process.

Table 1. Operating conditions for a centrifugal pump in the cooling circuit of a high performance gasoline car.

Angular velocity	N	7500	rpm
Volumetric flow rate	$\dot{Q}$	440	lpm
Total pressure head	Δp_t	3.5	bar
Temperature	T	95	°C
Density	ρ	1023.5	kg/m^3
Kinematic viscosity	ν	0.815	mm^2/s

The geometrical constraints, in general, are stringent and can be ascribed to packaging limitations and to feasibility requirements. The packaging constraints vary with the working point and the application, e.g., the maximum impeller diameter varies in a range from 30 to 90 mm. Table 2 summarizes the constraints for this case. The feasibility requirements depend on the manufacturing technology. The molding, mostly used for the pump manufacture, requires a minimum blade thickness of 2 mm and a minimum outlet blade angle.

Table 2. Maximum value for some pump geometric parameters prescribed by packaging constraints

Impeller outlet diameter	D_2	80 mm
Impeller outlet blade height	b_2	13 mm
Radial overall dimension	-	160 mm

3. Geometry Parametrization

Automotive centrifugal pumps are made up of three main components, i.e., the impeller, the vaneless diffuser, and the volute, as shown in Figure 1. The main symbols adopted in this work are reported in Figure 2, where D_0 is the inlet pipe diameter, $D_{1,h}$ and $D_{1,s}$ are the leading edge impeller diameter at the hub and shroud, D_2 is the impeller outer

diameter, b_2 is the blade height at the impeller outlet, D_3 and b_3 are the outlet diameter and width of the vaneless diffuser, β_{b1} and β_{b2} are the angles of the camber line at impeller inflow and outflow, γ is the stagger angle, and δ_s is the relative twisting angle of the leading edge at shroud with respect to the hub.

Impeller, vaneless diffuser and volute are parameterized through Bézier curves and surfaces with the open-source software Scilab [12], and 21 design variables (DVs) are adopted: 17 for the impeller (DV_i), 2 for the vaneless diffuser (DV_d), and 2 for the volute (DV_v). Table 3 summarizes the DVs adopted in this optimization methodology, which are described in detail in Sections 3.1 and 3.2. The DVs can include functions of the geometrical parameters chosen to drive the optimization process or explicitly their values.

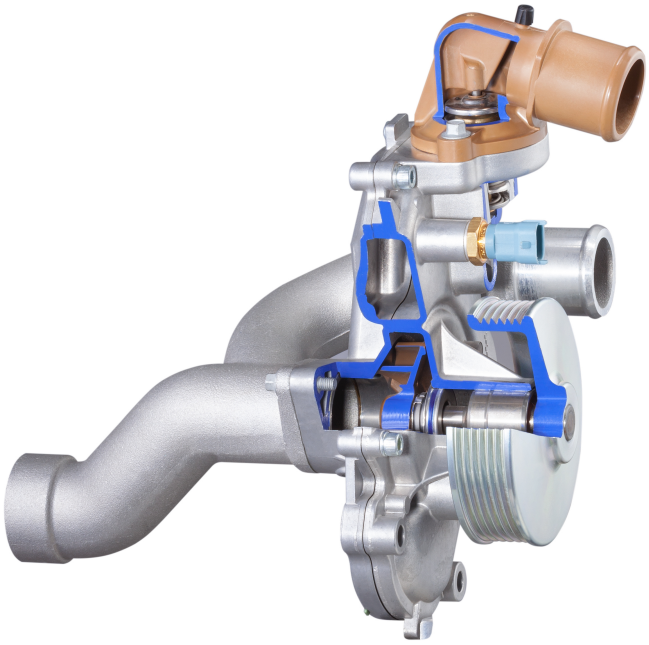

Figure 1. Centrifugal pump assembly (courtesy of Industrie Saleri Italo S.p.A.) for engine cooling circuits.

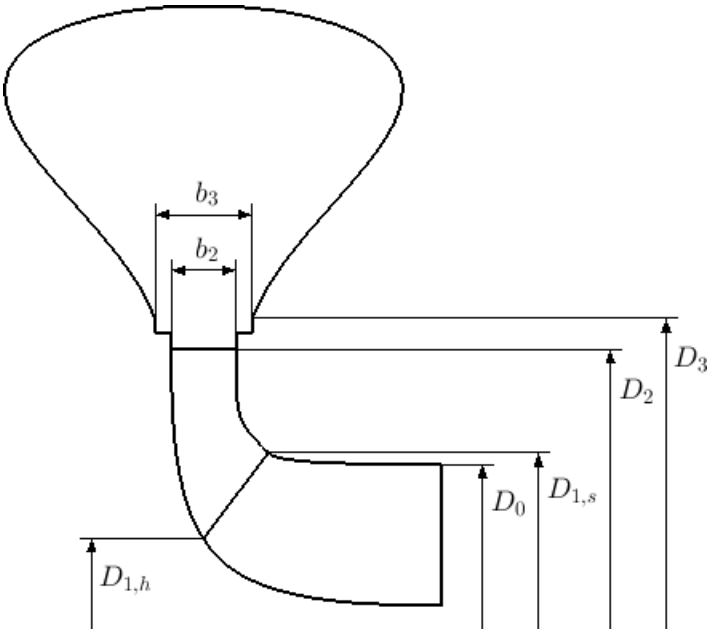

Figure 2. *Cont.*

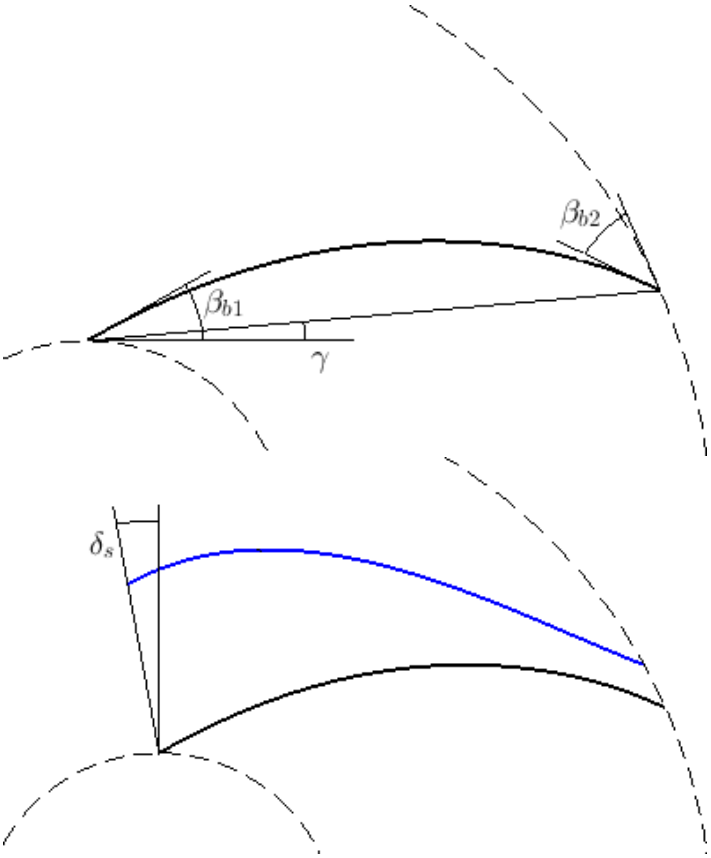

Figure 2. Main symbols for the impeller geometry (**top**), and impeller blade (**middle**, **bottom**).

3.1. Impeller

The impeller geometry considered in this parametrization has an axial inflow and a radial outflow. The parametrization is based on 17 DVs, which can be divided in four sub-sets: 3 DVs define the external dimensions of the impeller ($DV_{i,a}$); 9 DVs define the camber line at the hub and shroud ($DV_{i,b}$); 4 DVs define the meridional channel ($DV_{i,c}$); 1 DV defines the number of blades ($DV_{i,d}$).

$DV_{i,a}$ includes the impeller outer diameter (D_2), the inlet pipe diameter (D_0), and the blade height at the impeller outlet, (b_2). The bearing diameter is fixed equal to 6 mm. $DV_{i,b}$ includes the impeller diameter at the leading edge for the hub, $D_{1,h}$, and the shroud, $D_{1,s}$, the blade angle at the inlet for the hub, $\beta_{b1,h}$, and the shroud, $\beta_{b1,s}$, the blade angle at the outlet for the hub, $\beta_{b2,h}$, and the shroud, $\beta_{b2,s}$, the stagger angle for the hub, γ_h, and the shroud, γ_s, and the relative twisting angle of the leading edge for the shroud with respect to the hub, δ_s. The blade profiles at hub and shroud are built from the camber line and a thickness function. The camber lines (their projection is described on a plane perpendicular to the rotation axis) are Bézier curves of fourth order (see Figure 3). The blade surface is defined as a linear interpolation between the profiles at hub and shroud.

The axial position of the control points 1, 2, 6, 7, i.e., z_1, z_2, z_6 and z_7 (see Figure 4) can be derived from $DV_{i,c}$ and are used to define the two Bézier curves adopted to represent the hub and the shroud for the meridional channel. The points 3, 4, 5 are fixed at $z = 0$ and points 8, 9, 10 at $z = b_2$ to obtain a radial outlet. The inlet channel before the blade is controlled by four control points: d and h correspond to the leading edge at the hub and shroud; points a, b, c and e, f, g are aligned in order to guarantee an axial inflow; furthermore, the axial position of points c and g is set to guarantee the continuity of the derivative of the meridional channel at the leading edge for both the hub and shroud.

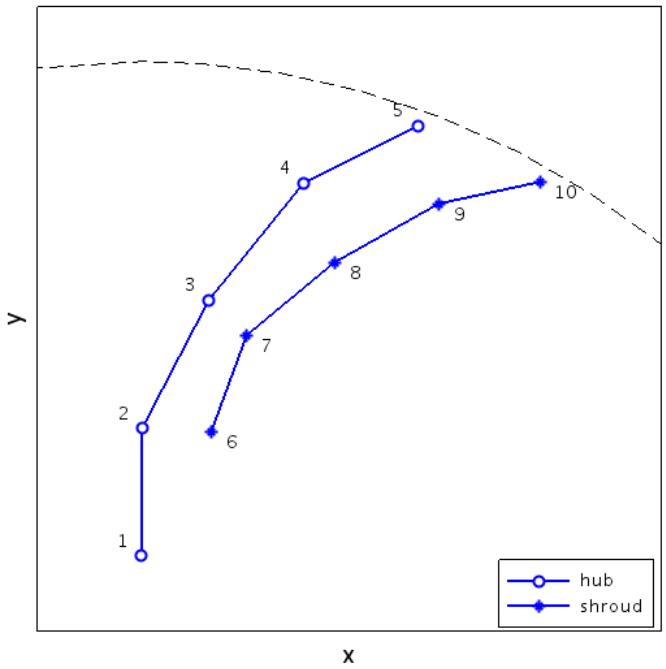

Figure 3. Control points for the camber surface at the hub and shroud.

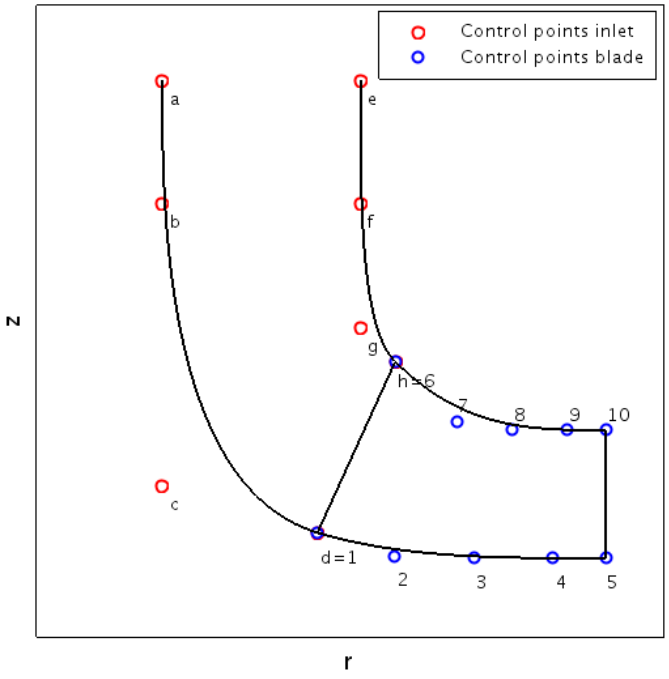

Figure 4. Control points for the meridional channel.

After defining the control points, the blade camber surface is generated (see Figure 5) and a thickness function is added (see Figure 6): the leading edge is defined with a symmetrical 4-digit NACA profile (NACA0012 has been adopted for this work) with a maximum thickness of 2 mm; when the maximum thickness is reached, this value is kept constant along the rest of the blade. The blade ends with a blunt trailing edge. The outlet of the impeller region is placed at 1 mm from the outer diameter D_2. $DV_{i,d}$ includes the number of impeller blades n_b.

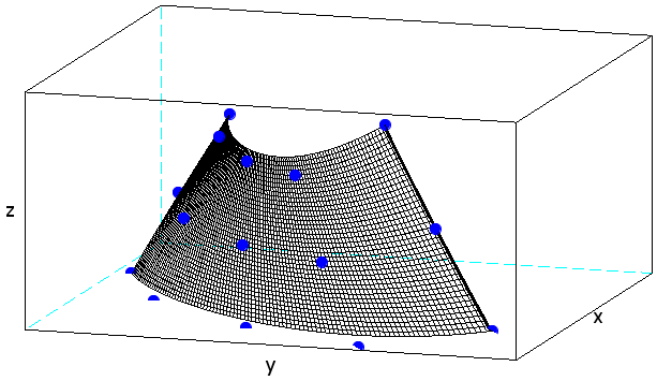

Figure 5. Control points and camber surface for the blade.

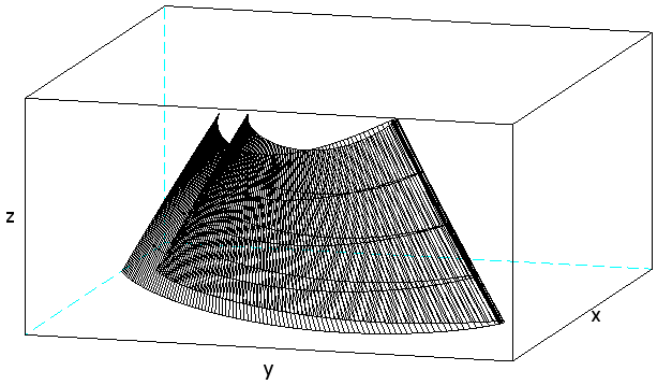

Figure 6. Pressure side and suction side of the blade after applying the thickness function.

3.2. Vaneless Diffuser and Volute

As reported in [1], the vaneless diffuser dimensions, the baffle tongue angle, and the area of the cross section at the volute outflow strongly affect the volute performance. The parametrization is based on 4 DVs. In particular, from DV_d, the outlet radius of the vaneless diffuser, R_3, and the diffuser width, b_3 (see Figure 7) can be obtained. DV_v includes the baffle tongue angle, α_i, and the cross section area at the volute outflow, A_4 (see Figure 8).

The constraints on R_3 and b_3 always guarantee the presence of a vaneless diffuser, characterized by $R_3 - R_2 = 1$ mm and $b_3 = b_2$. The volute geometry is built starting from the area of the cross section at the outflow. The shape of the cross section is the symmetrical horseshoe-shaped type, commonly adopted in commercial pumps [13] for its good performance. Finally, a linear interpolation is used to define the cross-section area from the outlet until the baffle tongue angle.

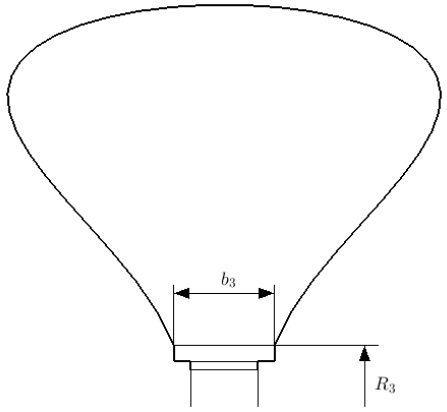

Figure 7. Vaneless diffuser width, b_3 and outlet radius, R_3.

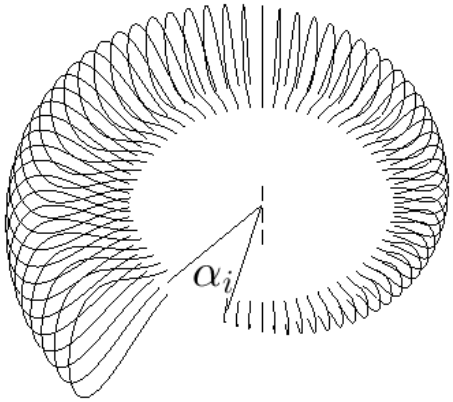

Figure 8. Baffle tongue angle controlled by the design variable α_i.

Table 3. List of the design variables (DVs) with the baseline values, the minimum/maximum values during the surrogate-based optimization (the percentage is computed with respect to the baseline value).

	Variable	Baseline	Min Value	Max Value
DV_i	D_2	70.1 mm	97%	103%
	D_0/D_2	0.589	95%	105%
	b_2	8.1 mm	90%	110%
	$\frac{D_2-D_{1,h}}{D_2-6}$	0.739	90%	110%
	$\frac{D_2-D_{1,s}}{D_2-D_0}$	1.00	90%	100%
	$\beta_{b1,h}$	29.5 °	92%	108%
	$\beta_{b1,s}-\beta_{b1,h}$	0 °	-5.0°	0.0°
	$\beta_{b2,h}$	40 °	94%	106%
	$\beta_{b2,s}$	40 °	94%	106%
	γ_h	85 °	88%	112%
	$\gamma_s-\gamma_h$	0 °	-2.5°	2.5°
	δ_s	0 °	-2.5°	2.5°
	$\frac{z_1}{b_2}$	0.5	0%	150%
	$\frac{4(z_2)}{z_1}$	1.0	0%	200%
	$\frac{z_6-b_2}{b_2}$	0.742	34%	101%
	$\frac{4(z_7-b_2)}{z_6-b_2}$	1.0	0%	200%
	n_b	6	5	7
DV_d	$R_3-D_2/2$	1.00 mm	0.00 mm	6.65 mm
	b_3/b_2	1.00	1.00	1.925
DV_v	A_4	907 mm^2	80%	120%
	α_i	30 °	100%	133%

4. CFD Setup

The mesh generation and the flow-field have been computed using the 2020 R2 release of ANSYS [14]. The ANSYS CFX solver is used to solve the incompressible RANS (Reynolds Average Navier Stokes) equations coupled with the SST (Shear Stress Tensor) turbulence model [15].

The impeller inlet section has been extruded along the axial direction to avoid possible disturbance at the inflow due to the blade leading edge. The length of the inlet pipe is $L = 3D_1$, where D_1 is the impeller inlet diameter. Only one blade passage is considered with periodic conditions.

The mesh of the impeller is generated using the software ANSYS TurboGrid, while the mesh of the volute is generated using ANSYS FLUENT Meshing. The size of the elements

adjacent to the solid walls is equal to an averaged non-dimensional distance $y^+ \approx 20$ and $y^+ \approx 4$ for the impeller and volute, respectively. CFX automatic wall treatment is applied to the blade wall, hub and shroud, i.e., CFX automatically switches from a wall function approach to a low Re approach, depending on the grid spacing near the wall.

At the domain inlet the volumetric flow rate $\dot{Q} = 7.33 \times 10^{-3}/\mathrm{m}^3/\mathrm{s}$, the turbulence intensity $Tu_0 = 4\%$, and the ratio $(\nu_t/\nu)_0 = 10$ are prescribed. The corresponding turbulent kinetic energy, k_0, and the specific dissipation rate, ω_0, are computed as

$$k_0 = \frac{3}{2} U_0^2 Tu_0^2,$$

$$\omega_0 = \frac{k_0}{\nu} \left(\frac{\nu_t}{\nu} \right)^{-1},$$

where $U_0 = 4\dot{Q}/(\pi D_0^2)$ is the inlet velocity. At the outflow a static pressure $p_4 = 0\ Pa$ is set. The no-slip adiabatic condition is applied to the blade walls, hub and shroud.

Steady-state simulations are performed using the multiple reference frame (MRF) approach, which implies no relative mesh motion between the rotating and stationary parts. In the rotating reference frame, where the relative velocity is computed, the momentum equation is modified, adding Coriolis and centrifugal terms. The interface between moving and fixed domain is treated using the mixing plane approach. This approach, unlike the frozen rotor interface, avoids the convection through the pump of non-physical wakes created by the impeller blades and remove the impact of the relative position between impeller blade and volute. Moreover, Fracassi et al. [16] demonstrated how this approach provides results in good agreement with unsteady simulations.

High resolution schemes are used for the velocity and the turbulent quantities.

Mesh Convergence Study

A mesh convergence study has been performed for the baseline geometry, using three grids with the number of elements ranging from 0.83 M to 3.09 M. In particular, Figure 9 shows a detail of the coarse (top-left), medium (top-right) and fine (bottom) mesh, while Figure 10 shows details of the impeller and volute medium mesh for the baseline geometry. The grid convergence study is summarized in Table 4, where the predicted pressure rise and efficiency are reported. As suggested by the convergence study, the grid with 1.53 M elements (medium) ensures a good compromise between computing time and accuracy of the results, and, therefore, it is chosen for the optimization.

Table 4. Grid convergence study for the baseline geometry. The quantities of interest are the static pressure rise, Δp, and the pump hydraulic efficiency, η.

Mesh	Elements	Elements_{imp}	Elements_{vol}	Δp [bar]	η
Coarse	0.83 M	0.10 M	0.73 M	3.321	0.853
Medium	1.53 M	0.26 M	1.27 M	3.453	0.875
Fine	0.83 M	0.50 M	2.59 M	3.483	0.877

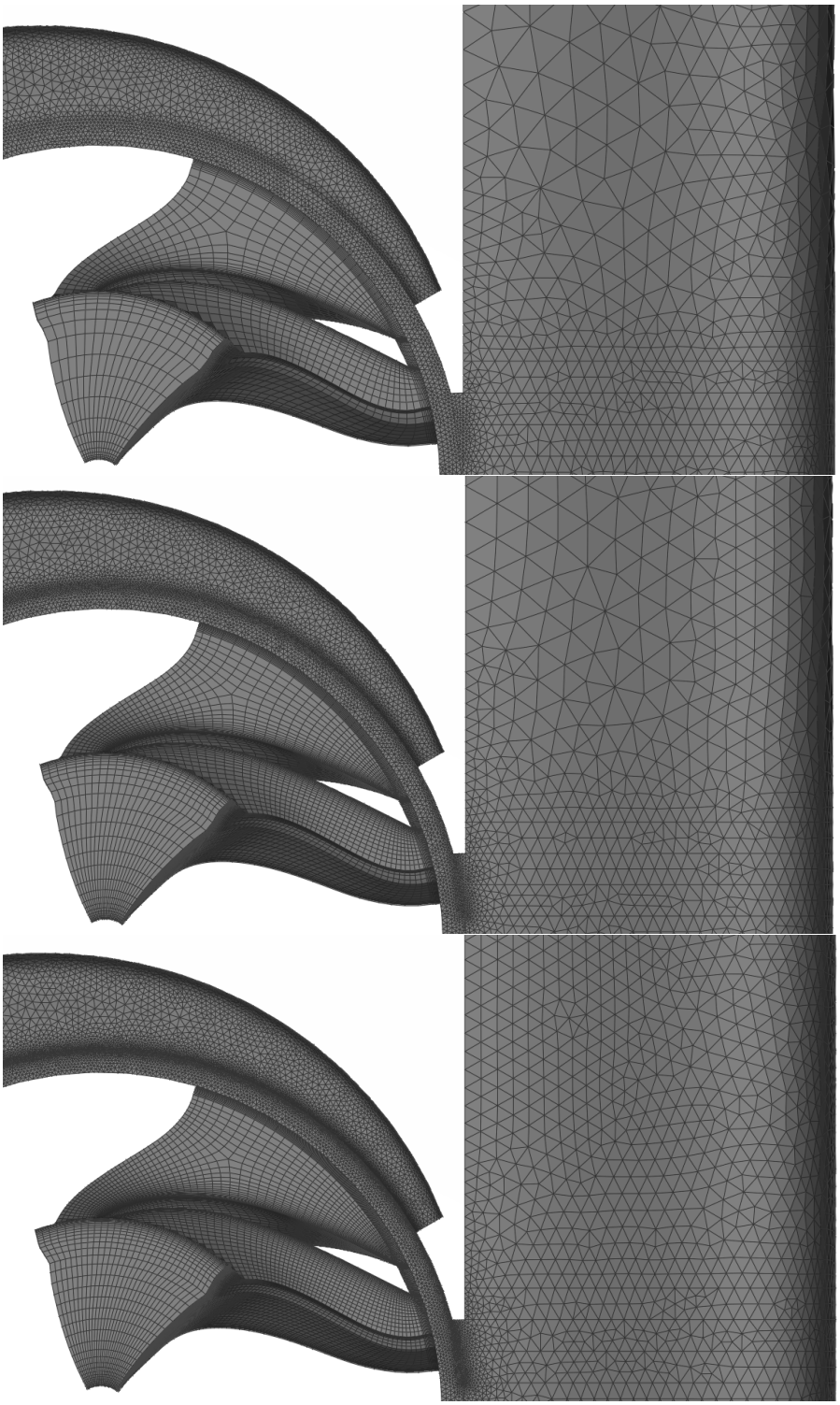

Figure 9. Detail of the coarse (**top**), medium (**middle**) and fine (**bottom**) mesh for the baseline design.

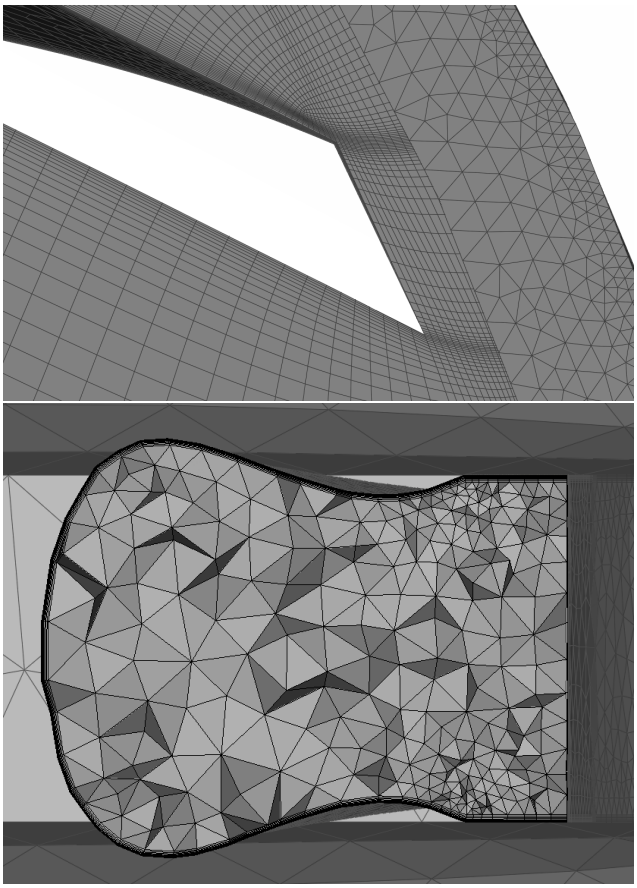

Figure 10. Detail of the impeller (**top**) and volute (**bottom**) mesh for the baseline design, medium mesh.

5. Optimization Strategy

Automotive companies require ever strict constraints in the design of centrifugal pumps, both in terms of size and coupling with the engine, which often lead to the manufacture of a new pump for each car model. As the design often starts from scratch, the design space becomes particularly large to explore, and, hence, a global optimization could require a huge computational cost, even if assisted by a surrogate model. As a consequence, the definition of a baseline design is of paramount importance. For this reason a lumped parameter (LP) code has been developed to provide the data to build the baseline 3D geometry, and to define the design space, which is used to perform a surrogate-based optimization (SBO). The SBO is based on a genetic algorithm assisted by a Kriging model. The flow chart of the proposed optimization strategy is reported in Figure 11.

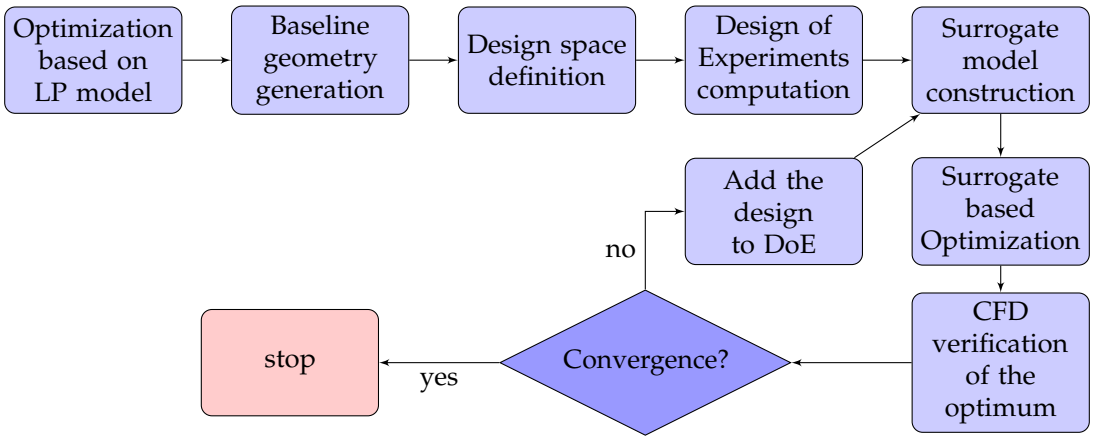

Figure 11. Flow chart of the optimization strategy.

5.1. Optimization Based on Lumped Parameter Model

The LP code for the preliminary design of the centrifugal pump with a volute casing is an extension of the approach proposed by Peck [17] (the procedure is reported in Appendix A), and is based on the following input parameters: the flow rate, $\dot{Q}$ [m^3/h], the pump head, H [m], the rotational speed, N [rpm], the number of impeller vanes, n_b, the impeller discharge angle, β_{b2} [°], the impeller thickness, t [m], the blade roughness, r [m], and the fluid kinematic viscosity, ν [m^2/s]. The output variables correspond to the DVs of the geometrical parametrization, reported in Table 3. Notice that the geometry respects the packaging constraints. Otherwise, it is necessary to increase the angular velocity with respect the initial requirement.

The hydraulic efficiency of the LP model is defined as a function of some DVs of the geometric parametrization, i.e., $\eta_{hyd} = f(b_1, b_2, D_1, D_2, A_4)$, and it is used to drive a cheap optimization based on a genetic algorithm.

The main geometrical parameters provided by the LP code, which are used to build the 3D model of the baseline design, are reported in Table 5.

Table 5. List of the geometrical parameters for the baseline and optimized geometries provided by the LP code and the SBO algorithm, respectively.

	Variable	Baseline	Optimum
Impeller	D_2	70.10 mm	68.00 mm
	D_0	41.29 mm	40.05 mm
	b_2	8.10 mm	7.90 mm
	$D_{1,h}$	22.73 mm	26.4 mm
	$D_{1,s}$	41.29 mm	42.76 mm
	$\beta_{b1,h}$	29.50°	28.40°
	$\beta_{b1,s}$	29.50°	23.50°
	$\beta_{b2,h}$	40.00°	37.60°
	$\beta_{b2,s}$	40.00°	42.40°
	γ_h	85.00°	91.05°
	γ_s	85.00°	89.86°
	δ_s	0.00°	−1.33°
	n_b	6	7
Vaneless diffuser	D_3	72.1 mm	74.48 mm
	b_3	8.1 mm	10.75 mm
Volute	A_4	907 mm^2	1043 mm^2
	α_i	30.00°	30.60°

5.2. Surrogate-Based Optimization

In literature, the single- (SOGA [18]) or multi-objective (MOGA [19]) genetic algorithms are used for turbomachinery shape optimization, due to their easiness and robustness: objective functions derivatives are not requested and the probability to remain trapped in a local optimum is very low. To alleviate the computational effort requested by genetic algorithms due to the large number of evaluations, the use of a surrogate model to approximate and evaluate the objective functions during the optimization process is mandatory. Both Kriging (KRG) [20,21] and artificial neural network (ANN) are used for the pumps optimization, even if De Donno et al. [18] show that KRG performs better than ANN in this context.

The KRG model performs a global approximation involving interpolation and the objective function is defined as:

$$\hat{f}(\underline{x}) = \underline{g}(\underline{x})^T \underline{\beta} + \epsilon(\underline{x}),$$

i.e., $\hat{f}$ is the sum of trend basis functions (here polynomials), which fits the DoE, and a stochastic function $\epsilon(x)$ with mean zero, which fixes the function to interpolate the experiments. $\underline{g}(\underline{x})$ is the vector of the basis functions, $\underline{\beta}$ is the vector of the generalized least squares estimates of the basis function coefficients and $\epsilon(x)$ is computed using a Gaussian correlation function.

The whole optimization strategy is managed by the Dakota [22] software and is summarized by the following steps:

1. Computation of a Design of Experiments (DoE) to create a training points database. The DoE is generated using the Latin Hypercube Sampling (LHS) method, which allows to randomly and uniformly distribute the designs over the whole design space. The DoE consists of $10N$ training points, where N is the number of design variables, as proposed by Jin et al. [23].
2. Training points evaluation. The points are evaluated using the CFD approach described in Section 4.
3. Surrogate models generation based on Kriging for the approximation of pump efficiency and pressure head.
4. Search for the maximum of the efficiency by means of the constrained SOGA applied to the surrogate model. Crossover rate and mutation rate are set equal to 0.8 and 0.1, respectively.
5. Verification of the maximum through a CFD simulation.
6. If the convergence criterion is not met, add the maximum to the training points database and return to step 3.

The iterative process described above improves continuously the surrogate accuracy and accelerates the optimization convergence. A global error is defined as

$$E = \frac{err_\eta}{max(\eta)} + \frac{err_{dp}}{\Delta p}, \tag{2}$$

where $err = |\hat{f} - f|$ is the error of the surrogate in evaluating the objective functions $\hat{f}$, i.e., the efficiency and the pressure head, with respect to the value f predicted by the CFD simulation. The convergence is considered to be reached when $E < tol_E$ ($tol_E = 0.05$ in this work) for at least ten iteration, and the maximum efficiency is not changed.

6. Results and Discussion

The DoE consists of 210 training points, but 38 designs have been rejected after their evaluation because of errors in the mesh generation or CFD calculation phase. The efficiency and the pressure head of these design are set to 0.8 and 3.2 bar, respectively, to force the search of the optimum far away. The analysis of the optimization convergence (see Figure 12) shows the absence of further unfeasible design.

Figure 12 shows the optimization convergence in terms of efficiency and pressure head. The SBO reaches the convergence after 68 iterations. Both values predicted by CFD and estimated by the Kriging model are reported. Figure 13 deeply investigates the optimization process in terms of the global error (see Equation (2)) and the achieved maximum efficiency. The global error shows a decreasing behaviour, while the efficiency reaches a value above 0.9 starting from 16-th iteration. The optimum design is characterized by $\eta = 0.905$, i.e., an improvement of 3% with respect to the baseline is achieved, and $\Delta p_t = 3.35$ bar.

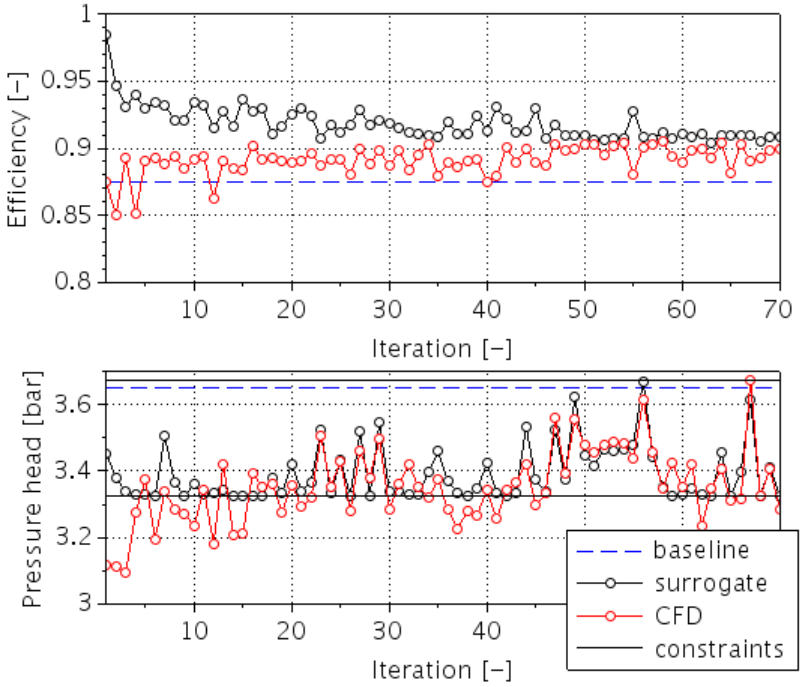

Figure 12. Evaluation of the design from the SOGA with the surrogate and CFD simulation: efficiency (**top**) and total pressure head (**bottom**).

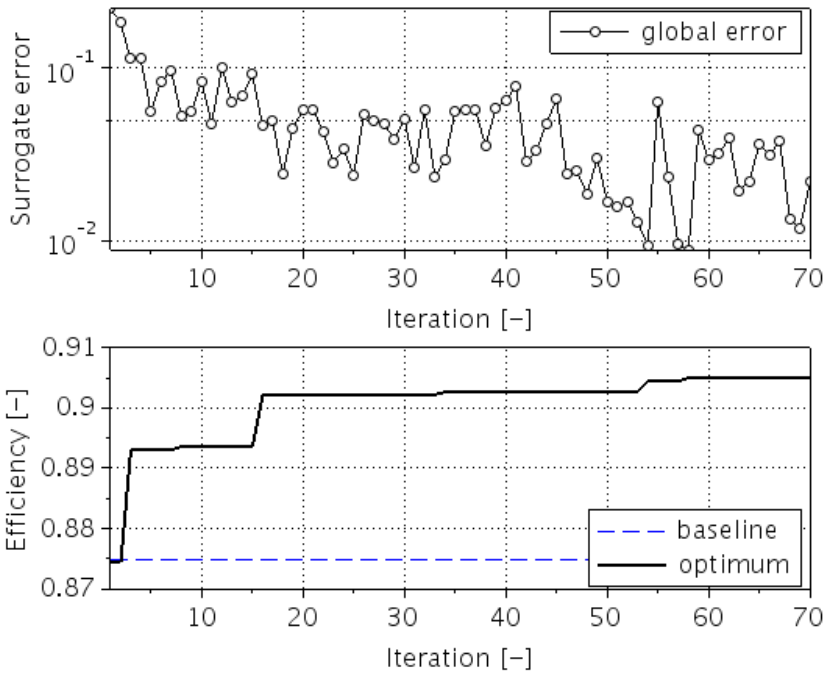

Figure 13. Convergence of the optimization strategy: global error (**top**) and maximum efficiency (**bottom**).

The profiles of the blade camberline in a conformal mapping plane are compared in Figure 14 for the baseline and optimal geometries. The abscissa of the coordinate system is

$$A(x_m) = \varphi(x_m) r(x_m),$$

where $x_m = \sqrt{z^2 + r^2}$ is the distance in the meridional direction (the blade leading edge is taken as origin), and represents also the ordinate, r is the distance from the rotation axis, and φ is the wrap angle, defined as

$$\varphi = \int_0^{L_m} \frac{dx_m}{r \tan(\beta_b)},$$

where β_b is the blade angle, and L_m the meridional distance between leading and trailing edge. Profiles at 0%, 50%, and 100% of the span are depicted. The baseline profile shows a constant distribution of β_{b1} and β_{b2} along the span, while a variation is appreciable for the optimized geometry.

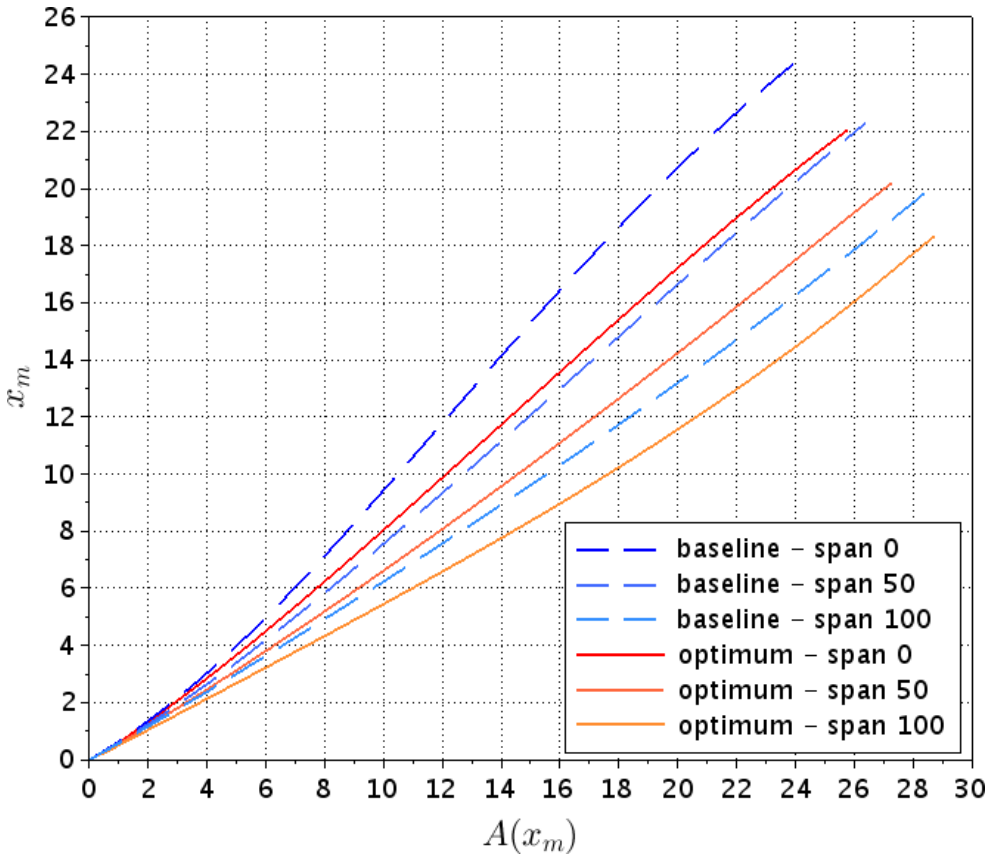

Figure 14. Profiles of the blade camberline in the conformal mapping plane for the baseline and optimized geometry.

The optimal geometry is compared with the baseline in Figure 15, where the blade profiles of the impeller at hub and shroud (right), the meridional channel (left), and the volute shape (bottom) at the outlet are shown. Figures 16–22 compare the flow field between the optimized and the baseline geometries to investigate the effect of the geometrical changes on the efficiency. Notice that maximize the efficiency corresponds to minimize the power at the impeller W, as the Δp_t is set at less than a tolerance.

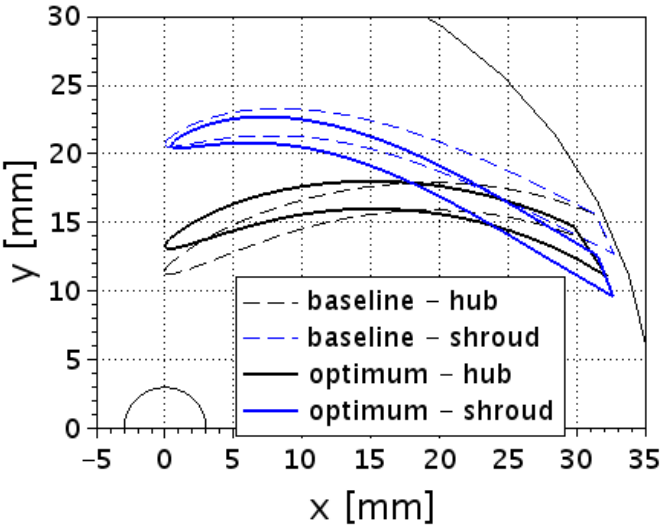

(**a**) *Impeller blade*

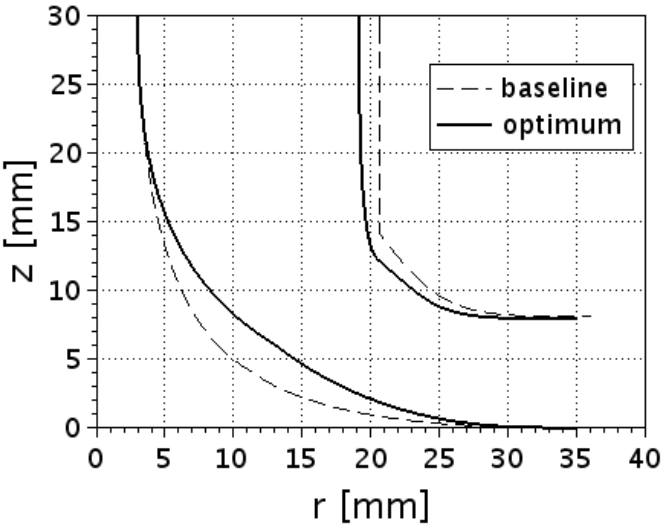

(**b**) *Meridional channel*

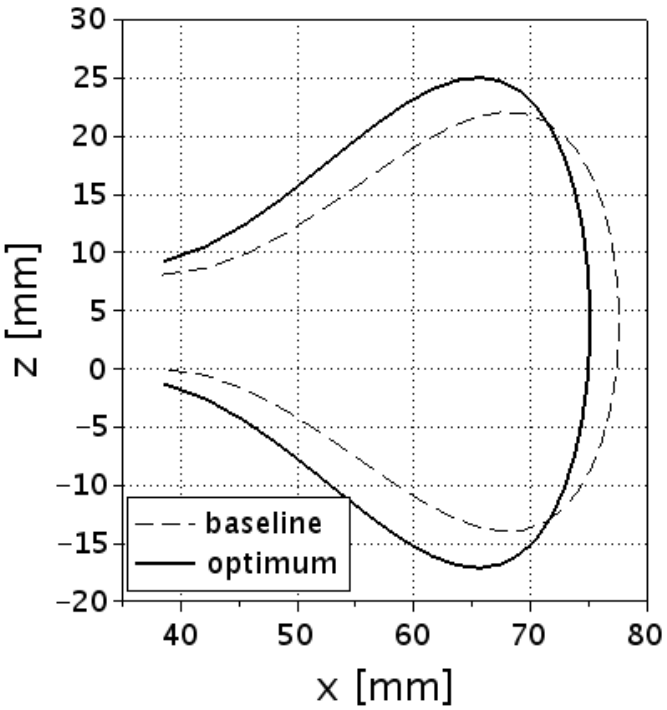

(**c**) *Volute outlet*

Figure 15. Comparison between baseline and optimized geometries.

Initially, the effect of the impeller blade geometry is investigated, comparing the pressure coefficient, c_p, and the skin friction coefficient, c_f, along the blade (see Figure 16) for the baseline and the optimal geometries. The coefficients are defined as follows:

$$c_p = \frac{2(p - p_o)}{\rho U_o^2} \qquad c_f = \frac{2\tau_{wall}}{\rho U_0^2}$$

where p_0 and U_0 are the static pressure and the velocity magnitude at the inlet pipe and τ_{wall} is the wall shear stress along the blade. The c_p distribution on the suction side shows a reduction of the pressure drop near the leading edge, while it assumes lower values on the pressure side. The area defined by the pressure and suction side curves is lower for

the optimal geometry, which corresponds to a decrease of the blade loading, and, as a consequence, of W. The difference in the friction coefficient c_f at the leading edge between the suction and pressure side is reduced in the optimal configuration; this discrepancy is motivated by an erroneous blade angle at the leading edge for the baseline. On the suction side a lower c_f distribution for the optimal geometry confirms a reduction of the losses. Figure 17 shows the static pressure at mid-span for the baseline (left) and optimized geometry (right). The pressure contours for the baseline are characterized by a low pressure area near the leading edge, which is completely removed in the optimal geometry, reducing also the cavitation problems. Figure 18 shows the velocity contours with streamlines at the plane $z = 5$ mm for the baseline (left) and optimized geometry (right). The small zone of acceleration near the leading edge of the suction side, probably motivated by a not correct blade inlet angle, is removed, and a smoother acceleration is visible in the blade channel. Finally, the wake near the trailing edge is reduced and the velocity distribution at the impeller outlet is more uniform.

The flow in the meridional channel is analyzed in Figure 19. The velocity contours show a more uniform distribution along the span in the inlet pipe and inside the impeller for the optimal geometry. This is obtained with a modification of the hub and shroud profile, as shown in Figure 15. In particular, the reduction of the section at the end of the inlet pipe avoids the stall at the hub. Moreover, at the impeller outlet the velocity peak is reduced and the velocity distribution is more uniform along the blade height.

Finally, the flow field in the volute is analyzed. In particular, Figures 20 and 21 show the pressure and velocity contours with streamlines in a plane at $z = 4$ mm. The pressure contours are quite similar for both baseline and optimized geometries. However, the latter shows a reduction of the low pressure zone at the volute tongue. The velocity contours show smaller values in the optimized geometry for the increased cross-section area (see Figure 22). Moreover, the small recirculation zone after the volute tongue is removed in the optimal geometry.

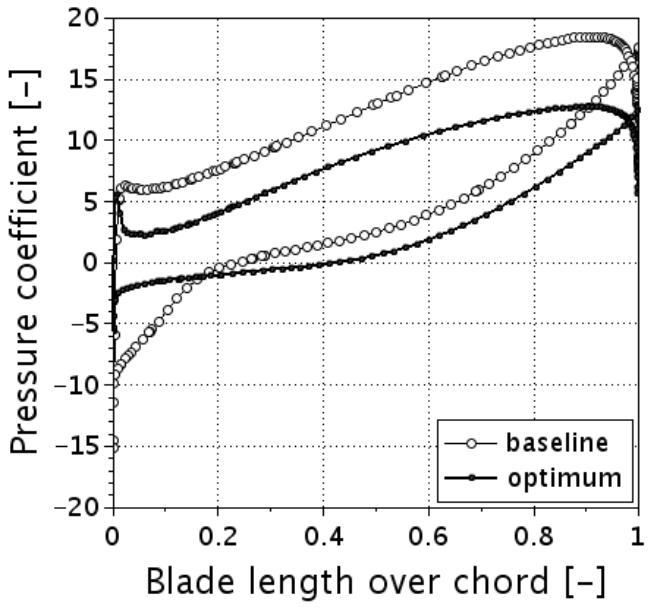

(**a**)

Figure 16. *Cont.*

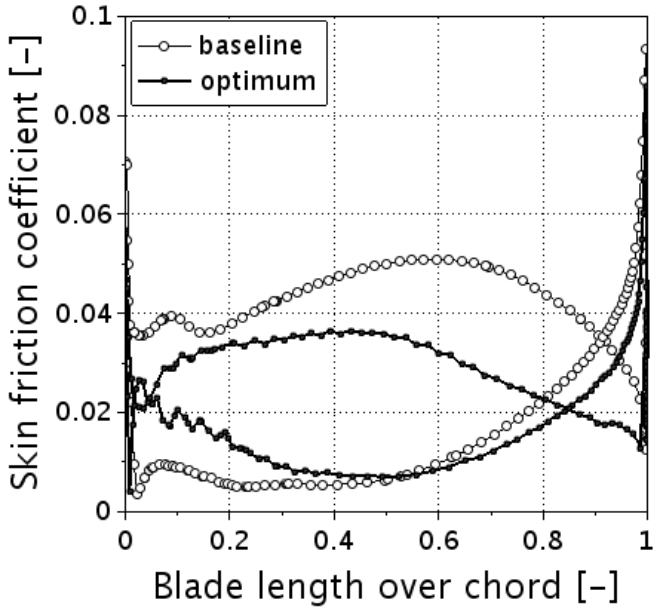

(**b**)

Figure 16. Pressure coefficient (**a**) and skin friction coefficient (**b**) along the blade for the baseline and the optimized geometry.

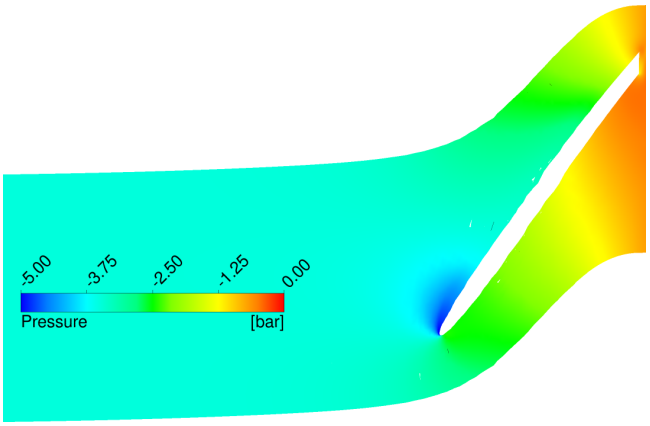

(**a**)

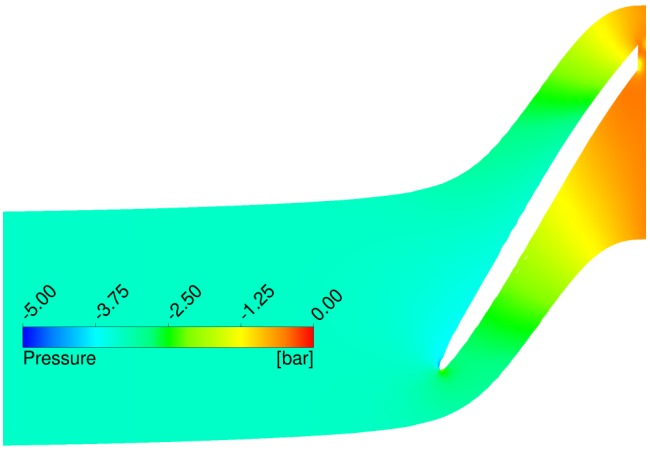

(**b**)

Figure 17. Static pressure field in the blade to blade view at 50% of the span for the baseline (**a**) and optimized (**b**) geometries.

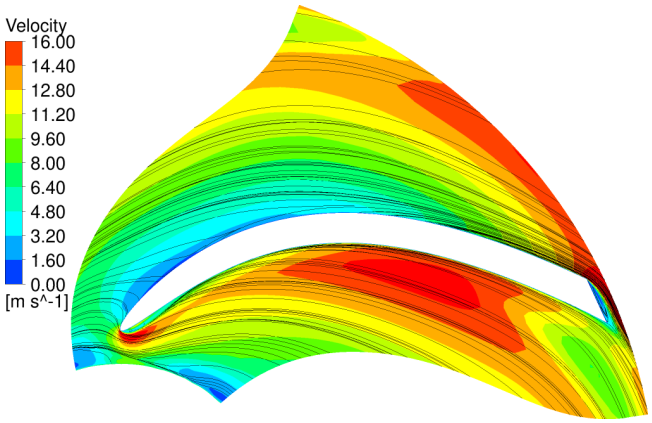

(**a**)

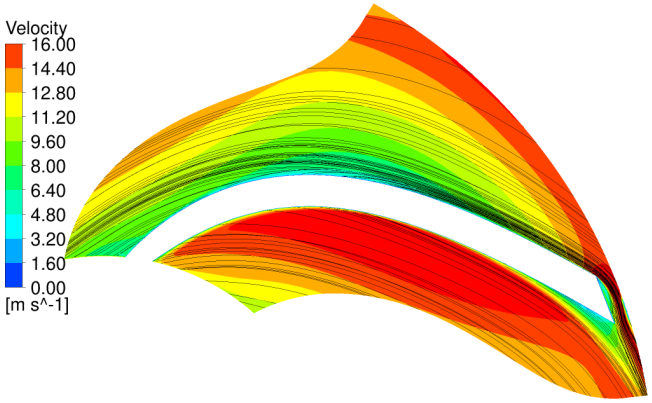

(**b**)

Figure 18. Velocity contours and streamline in the plane z = 5 mm for the baseline (**a**) and the optimized (**b**) geometries.

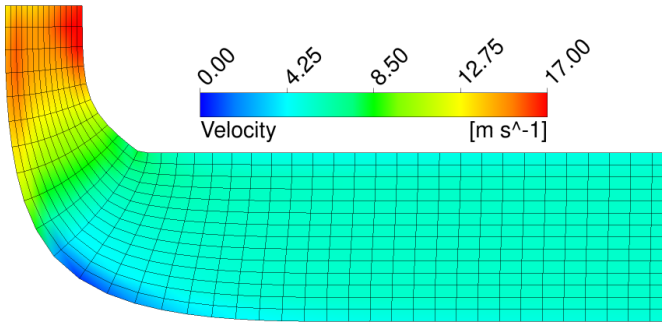

(**a**)

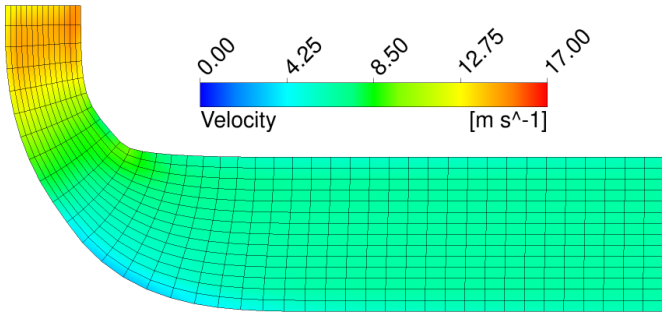

(**b**)

Figure 19. Velocity field in the meridional channel for the baseline (**a**) and the optimized (**b**) geometries.

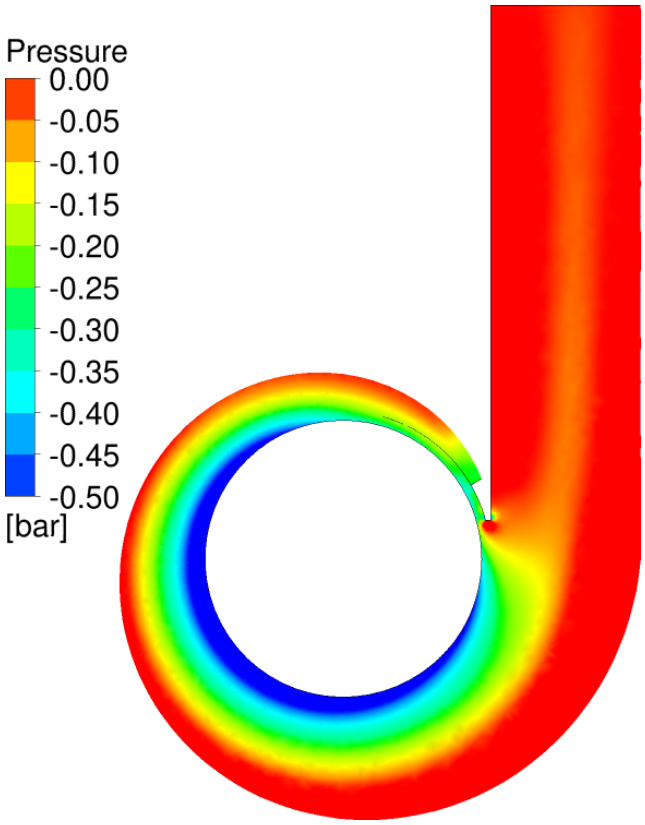

(**a**)

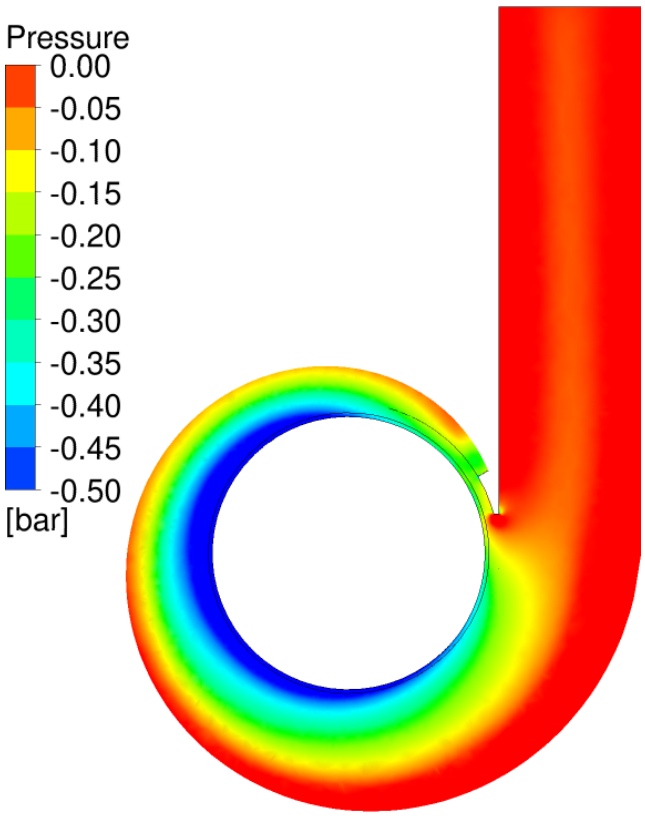

(**b**)

Figure 20. Static pressure field in the volute at $z = 4$ mm for the baseline (**a**) and the optimized (**b**) geometries.

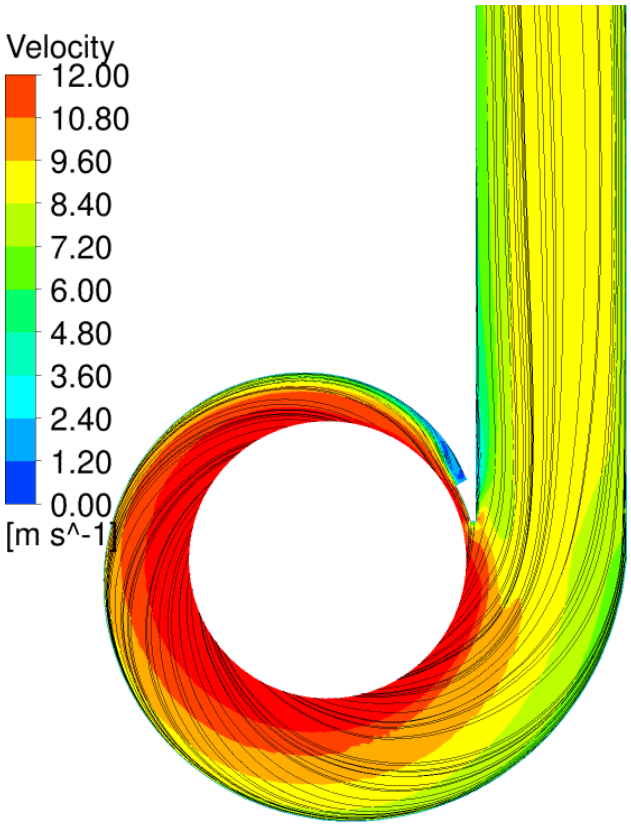

(**a**)

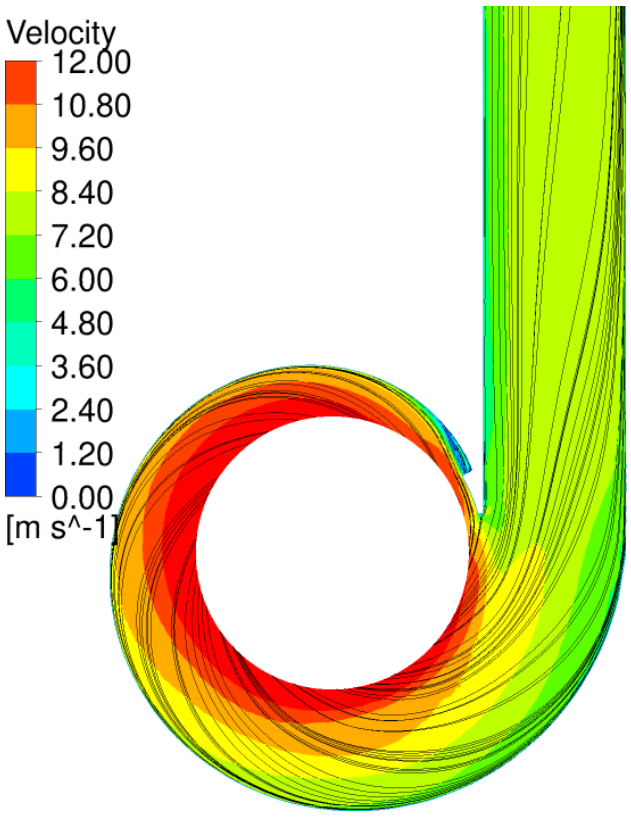

(**b**)

Figure 21. Velocity field and streamlines in the volute at $z = 4$ mm for the baseline (**a**) and the optimized (**b**) geometries.

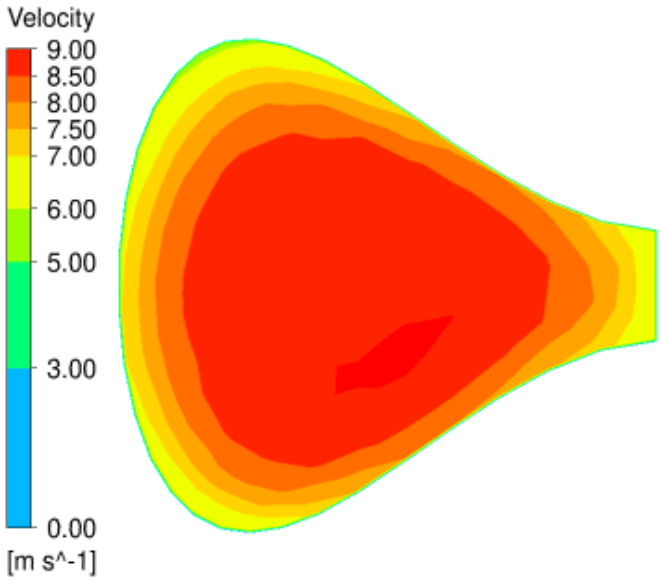

(**a**)

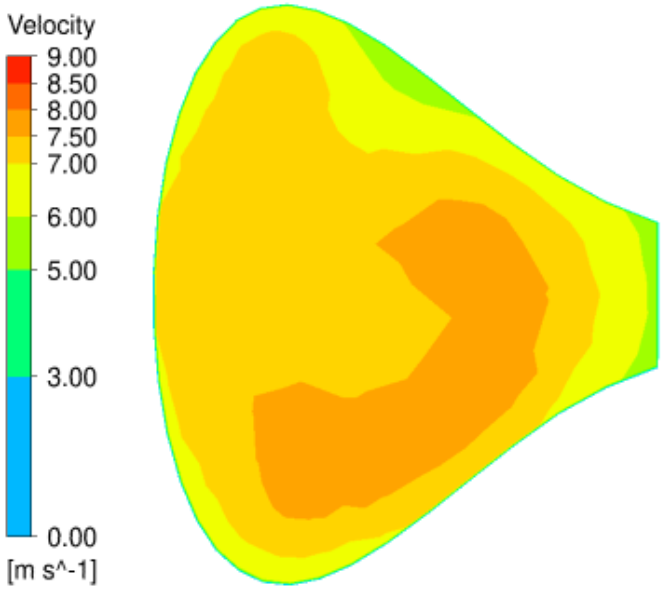

(**b**)

Figure 22. Velocity field at the volute outlet for the baseline (**a**) and the optimized (**b**) geometries.

The distribution of the velocity vectors for the baseline and optimized geometry is displayed in Figure 23 for a plane at $z = 5$ mm. A small recirculation zone is evident near the leading edge of the baseline geometry, while the optimized geometry is characterized by a smooth distribution of the vectors.

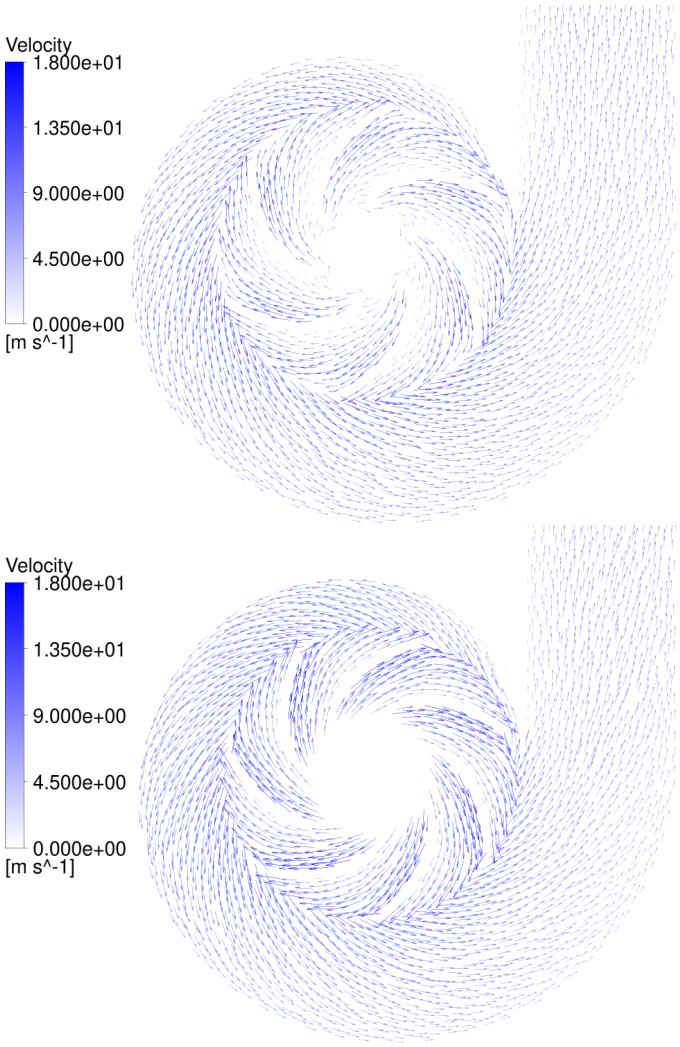

Figure 23. Velocity vectors (relative velocity for the impeller and absolute velocity for the volute) for the baseline (**top**) and the optimized (**bottom**) geometries, $z = 5$ mm.

A comparison of the baseline and the optimal design in terms of the static pressure rise, Δp, total pressure rise, Δp_t and hydraulic efficiency is reported in Table 6. Moreover, also single components, i.e., impeller, vaneless diffuser and volute, are compared. The global efficiency is increased by 3%; this improvement has been obtained decreasing the power absorbed by the impeller, and slightly the total pressure rise. The impeller torque C (and the power at the impeller W) is reduced by 11% in the optimal design, and its efficiency, $\eta_{imp} = \dot{Q}\Delta p_{t,imp}/\mathrm{W}$, is increased by 3%. The reduction of C can be ascribed to the decrease of the blade loading, as shown in Figure 16 by the c_P distribution, and of the losses. In particular, lower losses were achieved modifying the shape of the impeller blade and of the meridional channel, as shown in Figures 17–19. The vaneless diffuser of the optimal design provides an increase of the static pressure head about 5% together with an halving of the total pressure losses. The higher static pressure rise is achieved increasing the radial size of the vaneless diffuser due to the reduction of the impeller outlet diameter D_2, and the increase of the diffuser outlet height, b_3. There is also a reduction of the total pressure losses, which can be ascribed to the lower velocity of the flow entering the diffuser, as shown in Figure 19. The optimization of the volute leads to a slightly decrease of the total pressure losses. In fact, a higher volute area leads to a lower velocity but a wider wet surface, which have an opposite effect of the friction losses. The recover of the static pressure is decreased due to a slower flow at the exit of the vaneless diffuser.

Table 6. Comparison of the baseline and the optimal design for the impeller, the vaneless diffuser and the volute. η_{imp} is the impeller efficiency, C the torque absorbed by the pump shaft, Δp the static pressure variation, Δp_{tot} the total pressure variation, η the pump hydraulic efficiency.

			Baseline	**Optimal**
Impeller	Δp_{imp}	[bar]	2.901	2.781
	$\Delta p_{t,imp}$	[bar]	3.887	3.555
	C	[Nm]	3.900	3.458
	η_{imp}	[-]	0.931	0.960
Diffuser	Δp_{dif}	[bar]	0.127	0.133
	$\Delta p_{t,dif}$	[bar]	−0.063	−0.030
Volute	Δp_{vol}	[bar]	0.426	0.391
	$\Delta p_{t,vol}$	[bar]	−0.173	−0.171
Global	Δp	[bar]	3.453	3.304
	Δp_t	[bar]	3.651	3.354
	η	[-]	0.875	0.905

7. Conclusions

A procedure for the automated design of a centrifugal pump for the cooling of car engines is presented. It involves a shape optimization of the impeller, vaneless diffuser and volute, with the objective of maximize the efficiency of the pump, keeping constant the operating conditions. The baseline geometry is obtained with a lumped parameter code. The baseline geometry is enhanced with a 3D surrogate based optimization.

The proposed approach demonstrates its robustness, as it provides for the prescribed operating condition a 3D design from scratch, which was optimized to enhance the pump hydraulic efficiency (η is increased by 3% at the end of the optimization).

The optimal design presents a decrease of the blade loading, and a smoother acceleration along the pressure side. Moreover, the low pressure area at the leading edge is reduced, and, consequently, the related cavitation problems. The velocity field across the meridional channel is modified by changing the hub and shroud profile to obtain a more uniform distribution. In particular, the reduction of the section at the end of the inlet pipe avoids the stall at the hub. Moreover, at the impeller outlet the velocity peak is reduced and the velocity distribution is more uniform along the blade height. In the volute the pressure distribution is quite similar for both designs. However, the optimal design shows a reduction of the low pressure zone at the volute tongue, and smaller velocity values for the increased cross-section area. Moreover, the small recirculation zone after the volute tongue is removed in the optimal geometry.

The components that have the greater impact to improving efficiency are the impeller and the vaneless diffuser. Only a slight improvement is obtained in the volute, probably for the reduced number of DVs used for its geometrical parametrization.

Each simulation has been run in parallel on 32 cores, and 1 h is needed to complete the workflow (mesh generation and CFD simulation). DoE required 210 simulations, while 68 iterations were needed by the optimization procedure to converge to an optimum design. The computational cost of the whole optimization process was approximately 280 h (≈12 days) on 32 cores.

Ongoing work is devoted to enhance the parametrization of the volute, and to reduce the global number of DVs with an active subspace technique.

Author Contributions: Conceptualization, A.G. and R.D.D.; methodology, A.F.; software, R.D.D.; validation, A.F. and A.M.; formal analysis, G.N. and A.M.; investigation, A.F.; resources, R.D.D. and A.M.; data curation, G.N.; writing—original draft preparation, A.F. and R.D.D.; writing—review and editing, A.G., G.N. and A.M.; visualization, G.N.; supervision, A.G. and R.D.D.; project administration, A.G. All authors have read and agreed to the published version of the manuscript.

Funding: This research received no external funding.

Acknowledgments: We thank Industrie Saleri Italo S.p.A., who provided the hardware and software resources used in this work.

Conflicts of Interest: The authors declare no conflict of interest.

Appendix A

The hydraulic and and pump efficiencies are initially estimated as a function of flow rate, $\dot{Q}$, the head, H, the roughness (through the coefficient K_h), and the specific speed, N_s, [17]:

$$\eta_h = 1 - \frac{K_h}{\left(\dot{Q}H^{1/2}\right)^{1/4}} \frac{1}{100}, \tag{A1}$$

and

$$\eta_P = 1 - \frac{11,000}{N_s} \frac{1}{100}, \tag{A2}$$

where K_h is a coefficient to take into account the effect of the roughness. In particular, $K_h = 32$ for small pumps (high roughness), $K_h = 28$ for medium pumps (medium roughness), and $K_h = 20$ for large pumps (low roughness). The specific speed is computed as:

$$N_s = 0.86 \frac{N\sqrt{\dot{Q}}}{H^{3/4}}. \tag{A3}$$

Initially, quantities at the impeller outlet are computed, i.e., the impeller diameter, D_2, the blade height, b_2, the outflow area, A_2, the meridional velocity c_{m2}, the blade velocity, u_2. The breadth ratio, $r_b = D_2/b_2$, is first evaluated as

$$r_b = \frac{K_b}{N_s}, \tag{A4}$$

where b_2 is the height of the impeller blade at the outlet, and K_b a coefficient that can assume the following values: $K_b = 15{,}000$ from a wider impeller, $K_b = 20{,}000$, and $K_b = 25{,}000$ for larger impeller. The theoretical head, i.e., under the hypothesis of axial inflow and an infinite number of impeller vanes, can be computed with the Euler equation as

$$H_{th} = \frac{u_2 c_{u2}}{g}, \tag{A5}$$

where g is the gravitational acceleration, u_2 the blade velocity at the impeller outlet,

$$u_2 = \frac{\pi N D_2}{60}, \tag{A6}$$

c_{u2} the whirl velocity, defined as

$$c_{u2} = u_2 - c_{m2} \cot \beta_{b2}. \tag{A7}$$

The meridional velocity, c_{m2}, at the impeller outflow is computed as

$$c_{m2} = \frac{\dot{Q}}{A_2}, \tag{A8}$$

where A_2 is the outflow area and can be computed (neglecting the blades thickness) as

$$A_2 = \pi D_2 b_2 = \frac{\pi D_2^2}{r_b}. \tag{A9}$$

The theoretical head, H_{th}, can be related also to the pump head, H, with the Pfleiderer [24] slip coefficient, p, as

$$H_{th} = \frac{H}{\eta_h}(1+p), \tag{A10}$$

where

$$p = K_s R, \tag{A11}$$

where K_s is the impeller slip constant, and can be chosen in the ranges 1.7–1.8 and 1.5–1.6 for flat and fully backed off impeller outlet tips, respectively. R is the blade loading ratio and can be defined as

$$R = \frac{9.55\dot{Q}}{n_b\left(\frac{D_2^3}{K_A}\right)N}, \tag{A12}$$

where K_A is the projected area coefficient and can be defined as

$$K_A = 50 + 4.5 r_b. \tag{A13}$$

Equating Equations (A5) and (A10), an equation of the form

$$A(1 + B/D_2^3) - CD_2^2 + F/D_2 = 0$$

is obtained, where A, B, C, and F are known constants. This equation can be solved iteratively, assuming a tentative value for D_2 that neglects the effects of the vanes number, the outlet angle, and can be computed from the following equation:

$$u_2 = \pi D_2 N/60 = K_{sp}\sqrt{2gH}, \tag{A14}$$

where K_{sp} is a speed coefficient defined as

$$K_{sp} = 1 + \frac{N_s}{20000}. \tag{A15}$$

Finally, the height of the blade, the area, the meridional velocity, and the blade velocity at the impeller outlet are given by:

$$b_2 = \frac{D_2}{r_b}, \tag{A16}$$

$$A_2 = \left(\pi D_2 - \frac{n_b t_2}{\sin\beta_{b2}}\right)b_2, \tag{A17}$$

$$C_{m2} = \frac{\dot{Q}}{A_2}, \tag{A18}$$

$$u_2 = \pi D_2 N/60. \tag{A19}$$

The following quantities at the impeller inlet are computed: the impeller diameter, D_1, the blade height, b_1, the inflow area, A_1, the meridional velocity c_{m1}, the blade velocity, u_1, and the blade angle, β_{b1}. From the eye velocity, $v_e = k_e c_{m2}$ ($1.3 < k_e < 1.5$), the eye diameter, D_e, is computed as

$$D_e = \sqrt{\frac{4A_e}{\pi}} = \sqrt{\frac{4\dot{Q}}{\pi v_e}}, \tag{A20}$$

and $D_e = D_1$ for this pump configuration. The inflow impeller angle, β_{b1}, can be computed as

$$\beta_{b1} = \arctan\left(\frac{c_{m1}}{u_1 - c_{u1}}\right), \tag{A21}$$

where c_{m1} is the meridional velocity at the impeller inlet, and is defined as

$$c_{m1} = k_1 c_{m2}, \tag{A22}$$

where $1.3 < k_1 < 1.5$, u_1 is the inlet blade velocity and is computed as

$$u_1 = \pi D_1 \frac{N}{60}. \tag{A23}$$

The inlet whirl velocity, c_{u1}, is defined as

$$c_{u1} = \sqrt{c_1^2 - c_{m1}^2}, \tag{A24}$$

where $c_1 = K_{qm} c_{m1}$ ($1.1 < K_{qm} < 1.2$), and the height of the blade can be computed as

$$b_1 = \frac{A_1}{\pi D_1} - n_b \frac{t_2}{\sin \beta_{b1}}. \tag{A25}$$

Finally, the main dimensions of volute casing are computed, neglecting the vaneless diffuser. The whirl velocity at the impeller outlet is computed as

$$c_{u2} = \frac{H_{th} - u_1 c_{u1}}{u_2 (1 + p)}. \tag{A26}$$

The velocity at the volute throat is computed as

$$c_4 = K_t \sqrt{2gH}, \tag{A27}$$

where

$$K_t = 0.8 - \frac{N_s^{1/3}}{K_h}, \tag{A28}$$

with $K_h = 27.8$. Applying the free vortex theory, the radius and the area at the volute throat can be computed as

$$R_4 = c_{u2} \frac{D_2}{2c_4}, \tag{A29}$$

$$A_4 = \frac{\dot{Q}}{c_4}. \tag{A30}$$

To include the design procedure in an optimization loop, it is necessary to redefine η_h as a function of the DVs used for the optimization. Impeller losses, l_{imp}, can be defined as the sum of two contribution, $l_{imp,mf}$ (mixing and friction losses) and $l_{imp,s}$ (shock losses). The mixing/friction contribution can be defined as

$$l_{imp,mf} = 4 c_d \frac{L_b}{D_h} \left(\frac{w_{ave}}{u_2} \right)^2, \tag{A31}$$

where c_D is the dissipation coefficient

$$c_d = (c_f + 0.0015)(1.1 + 4 b_2^*), \tag{A32}$$

where $b_2^* = b_2 / D_2$, and c_f is the friction coefficient

$$c_f = \left\{ \frac{0.136}{\left[-\log\left(0.2 \frac{\epsilon}{L_b} + \frac{12.5}{Re} \right) \right]} \right\}^{2.15}, \tag{A33}$$

where $\epsilon = 0.00005\ m$ is the roughness, L_b the blade length, which is approximated as $L_b \approx D_2 - (D_1 - D_r)/2$, $Re = w_{ave} L_b/\nu$ the Reynolds number, ν the kinematic viscosity, and w_{ave} is the average relative velocity across the impeller

$$w_{ave} = \frac{2\dot{Q}}{a_1 b_1 + a_2 b_2}, \tag{A34}$$

where a_1 and a_2 are the distance between vanes at the leading and trailing edge, respectively, and can be generally defined as

$$a_i = \left(\pi D_i - \frac{n_b t}{\sin \beta_{bi}}\right) \sin \beta_{bi}. \tag{A35}$$

The hydraulic diameter, D_h, is defined as

$$D_h = \frac{2(a_1 b_1 + a_2 b_2)}{a_1 + b_1 + a_2 + b_2}. \tag{A36}$$

The shock contribution can be defined as

$$l_{imp,s} = 0.3 \left(\frac{w_1 - w_{q1}}{u_2}\right)^2, \tag{A37}$$

where $w_1 = \sqrt{c_{m1}^2 + (u_1 - c_{u1})^2}$ is the relative velocity at impeller leading edge, $w_{q1} = \dot{Q}/(n_b a_1 b_1)$ the velocity at the impeller throat, and $c_{u1} = c_{m1}/\tan \alpha_1$ the inlet whirl velocity. This loss term is active only if $w_{q1}/w_1 > 0.65$.

In this work only the friction contribution, $l_{vol,f}$, to volute losses is considered, and is computed approximating the volute volume as i sub volumes (with lateral surface $A_{l,i}$)

$$l_{vol} = l_{vol,f} = \frac{1}{\dot{Q} u_2^2} \sum_i \left[\left(c_f + 0.0015\right) c_i^3 \Delta A_i\right], \tag{A38}$$

where $c_i = c_{u3} r_3 / r_i \cos \alpha_3$ is the velocity of the flow through the i-th sub volume.

Finally the hydraulic efficiency is recomputed as

$$\eta_h = \frac{H}{H + l_{imp} + l_{vol}}, \tag{A39}$$

and the design process is repeated iteratively with the new η_h.

References

1. Han, X.; Kang, Y.; Sheng, J.; Hu, Y.; Zhao, W. Centrifugal pump impeller and volute shape optimization via combined NUMECA, genetic algorithm, and back propagation neural network. *Struct. Multidiscip. Optim.* **2019**, *61*. [CrossRef]
2. Nourbakhsh, A.; Safikhani, H.; Derakhshan, S. The comparison of multi-objective particle swarm optimization and NSGA II algorithm: Applications in centrifugal pumps. *Eng. Optim.* **2011**, *43*, 1095–1113. [CrossRef]
3. Shim, H.S.; Kim, K.Y. Design Optimization of the Impeller and Volute of a Centrifugal Pump to Improve the Hydraulic Performance and Flow Stability. *J. Fluids Eng.* **2020**, *142*. [CrossRef]
4. Derakhshan, S.; Pourmahdavi, M.; Abdolahnejad, E.; Reihani, A.; Ojaghi, A. Numerical shape optimization of a centrifugal pump impeller using artificial bee colony algorithm. *Comput. Fluids* **2013**, *81*, 145–151. [CrossRef]
5. Xu, Y.; Tan, L.; Cao, S.; Qu, W. Multiparameter and multiobjective optimization design of centrifugal pump based on orthogonal method. *Proc. Inst. Mech. Eng. Part J. Mech. Eng. Sci.* **2017**, *231*, 2569–2579. [CrossRef]
6. Derakhshan, S.; Bashiri, M. Investigation of an efficient shape optimization procedure for centrifugal pump impeller using eagle strategy algorithm and ANN (case study: Slurry flow). *Struct. Multidiscip. Optim.* **2018**, *58*, 459–473. [CrossRef]
7. Shim, H.S.; Kim, K.Y.; Choi, Y.S. Three-Objective Optimization of a Centrifugal Pump to Reduce Flow Recirculation and Cavitation. *J. Fluids Eng.* **2018**, *140*, 091202. [CrossRef]
8. Pei, J.; Wang, W.; Osman, M.; Gan, X. Multiparameter optimization for the nonlinear performance improvement of centrifugal pumps using a multilayer neural network. *J. Mech. Sci. Technol.* **2019**, *33*. [CrossRef]

9. Wang, W.; Yuan, S.; Pei, J.; Zhang, J. Optimization of the diffuser in a centrifugal pump by combining response surface method with multi-island genetic algorithm. *Proc. Inst. Mech. Eng. Part J. Process. Mech. Eng.* **2015**, *231*. [CrossRef]
10. Martin, H.; Rudiger, S. Genetic Algorithm Optimization of the Volute Shape of a Centrifugal Compressor. *Int. J. Rotating Mach.* **2016**, *2016*. [CrossRef]
11. De Donno, R.; Fracassi, A.; Noventa, G.; Ghidoni, A.; Rebay, S. Surrogate-Based Shape Optimization of Centrifugal Pumps for Automotive Engine Cooling Systems. *Comput. Methods Appl. Sci.* **2021**, *55*, 277–290. [CrossRef]
12. *Scilab*, 5.5.2 Ed. Available online: http://www.scilab.org (accessed on 12 November 2021).
13. Japikse, D.; Marscher, W.D.; Furst, R.B. *Centrifugal Pump Design and Performance*; Concepts ETI, Inc.: Wilder Vermont, VT, USA, 1997.
14. *ANSYS*, 1.1.1 Ed. Available online: https://www.ansys.com/ (accessed on 12 March 2021).
15. Menter, F. Zonal Two Equation k-w Turbulence Models For Aerodynamic Flows. *AIAA Pap.* **1993**, *1993*. [CrossRef]
16. Fracassi, A.; De Donno, R.; Ghidoni, A.; Congedo, P.M. Shape optimization and uncertainty assessment of a centrifugal pump. *Eng. Optim.* **2020**, 1–18. [CrossRef]
17. Peck, J.F. Design of Centrifugal Pumps with Computer Aid. *Proc. Inst. Mech. Eng.* **1968**, *183*, 321–351. [CrossRef]
18. De Donno, R.; Ghidoni, A.; Noventa, G.; Rebay, S. Shape optimization of the ERCOFTAC centrifugal pump impeller using open-source software. *Optim. Eng.* **2019**, *20*. [CrossRef]
19. Olivero, M.; Pasquale, D.; Ghidoni, A.; Rebay, S. Three-dimensional turbulent optimization of vaned diffusers for centrifugal compressors based on metamodel-assisted genetic algorithms. *Optim. Eng.* **2013**, *15*, 973–992. [CrossRef]
20. Brown, S.; Swiler, L.; Eldred, M.; Cyr, E.; Giunta, A.; Richards, M. The Surfpack Software Library for Surrogate Modeling of Sparse Irregularly Spaced Multidimensional Data. In Proceedings of the 11th AIAA/ISSMO Multidisciplinary Analysis and Optimization Conference, Portsmouth, WV, USA, 6–8 September 2006; Volume 3. [CrossRef]
21. De Donno, R.; Rebay, S.; Ghidoni, A. Surrogate-Based Shape Optimization of the ERCOFTAC Centrifugal Pump Impeller. *Comput. Methods Appl. Sci.* **2019**, 227–246. [CrossRef]
22. *Dakota*, 6.8 Ed. Available online: https://dakota.sandia.gov/ (accessed on 12 March 2021).
23. Jin, R.; Simpson, T. Comparative Studies Of Metamodeling Techniques Under Multiple Modeling Criteria. In Proceedings of the 8th Symposium on Multidisciplinary Analysis and Optimization, Long Beach, CA, USA, 6–8 September 2000. [CrossRef]
24. Pfleiderer, C. *Die Kreiselpumpen für Flüssigkeiten und Gase*, 5th ed.; Springer: Berlin/Heidelberg, Germany, 1961.